Geophysical Journal International

Geophys. J. Int. (2023) **232,** 1803–1820 https://doi.org/10.1093/gji/ggac414
Advance Access publication 2022 October 21
GJI Marine Geosciences and Applied Geophysics

Time-domain poroelastic full-waveform inversion of shallow seismic data: methodology and sensitivity analysis

Tingting Liu and Thomas Bohlen

Geophysical Institute, Karlsruhe Institute of Technology (KIT), Karlsruhe 76187*, Germany. E-mail:* tingting.liu@kit.edu

Accepted 2022 October 21. Received 2022 September 5; in original form 2022 May 23

SUMMARY

Full-waveform inversion (FWI) is considered as a high-resolution imaging technique to recover the geophysical parameters of the elastic subsurface from the entire content of the seismic signals. However, the subsurface material properties are less well estimated with elastic constraints, especially for the near-surface structure, which usually contains fluid contents. Since Biot theory has provided a framework to describe seismic wave propagations in the poroelastic media, in this work, we propose an algorithm for the 2-D time-domain (TD) poroelastic FWI (PFWI) when the fluid-saturated poroelastic equations are applied to carve the physical mechanism in the shallow subsurface. To detect the contribution of the poroelastic parameters to shallow seismic wavefields, the scattered *P*-*SV*&*SH* wavefields corresponding to a single model parameter are derived explicitly by Born approximation and shown numerically afterward. The Fréchet kernels are also derived and exhibited in *P*-*SV*&*SH* schemes to analyse the sensitivities of the objective function to different poroelastic parameters. Furthermore, we verify the accuracy of the derivations through model parameter reconstructions. We perform a series of numerical tests on gradients with respect to different model parameters to further evaluate inter-parameter trade-offs. PFWI holds potential possibilities to directly invert fluid-related physical parameters of the shallow subsurface.

Key words: Permeability and porosity; Waveform inversion; Surface waves and free oscillations; Wave scattering and diffraction.

1 INTRODUCTION

The accurate estimation of the Earth's subsurface properties is a challenging task for seismic exploration. Since seismic waves carry the underground structural heterogeneities information, full-waveform inversion (FWI) has become a multiparameter reconstruction technique that can exploit the entire information contents of seismograms (Virieux & Operto 2009). In general, the main interest in seismic detection is to extract the information of the physical material properties (e.g. lithology, porosity and fluid content) from different seismic attributes (e.g. *P*- and *S*-wave velocities) based on rock physical relations (Butler 2005). To extend FWI into the application of seismic reservoir characterization, Queißer & Singh (2013) employ the Gassmann model to relate *P*-wave velocity with CO_2 saturation directly in order to estimate CO_2 storage (Gassmann 1951). Dupuy *et al.* (2016) adopt a two-step workflow based on acoustic FWI to estimate rock-physics properties by inverting the effective medium properties. Hu *et al.* (2021) attempt to link the elastic properties with different rock-physics models to recover fluid properties (e.g. porosity ϕ) through elastic FWI. However, the rock properties related to the fluid information from the fluid-filled subsurface are still poorly considered by the elastodynamic FWI. The near-surface sediments are usually unconsolidated and composed of solid and fluid components. How to exploit the fluid information directly from the seismic waveforms has still not attracted enough attention.

Over the past decades, Biot's theory (Biot 1956a, b; Biot & Willis 1957) has been widely used as a reliable model to govern the poroelastic response since they build a framework relating poroelastic parameters to the seismic wave properties (Zhu & McMechan 1991; Masson *et al.* 2006; Morency & Tromp 2008). Morency *et al.* (2009) present sensitivity kernels for specific parametrizations in the poroelastic model based on adjoint methods. De Barros *et al.* (2010) introduce Biot's theory into frequency-domain FWI, which is limited to utilizing reflected waves. Yang *et al.* (2018) discuss the radiation patterns for different parametrizations in poroelastic media and implement several synthetic reconstruction tests based upon frequency-domain poroelastic FWI (Yang & Malcolm 2020). However, it is still an open question for time-domain (TD) FWI to directly employ Biot's theory to describe the physical mechanism of the near-surface structure.

This paper aims to introduce Biot's theory into the direct description of the shallow subsurface and make preparation for shallow-seismic TD poroelastic FWI (TD-PFWI). In Section 2, we first outline the fluid-saturated poroelastic equations and show the shallow seismic *P*-*SV*&*SH*

poroelastic wavefields numerically. In Section 3, We derive the explicit scattered wavefields of different poroelastic parameters in *P-SV&SH* patterns based on the high-frequency approximation (Wu & Aki 1985). The scattered wavefields corresponding to different model parameters are simulated numerically to investigate the sensitivities of the model parameters. In Section 4, we use the classic least-squares error functional as the objective function and derive the Fréchet kernels with respect to different poroelastic parameters (Tarantola & Valette 1982). Besides, the Lagrangian augmented functional (Plessix 2006) is explained to derive the adjoint poroelastic wavefields. Furthermore, we present the sensitivity kernels of different poroelastic parameters from the views of *P-SV&SH*, and implement a series of reconstruction tests on the synthetic Rayleigh/Love-wave data to justify the accuracy and feasibility of PFWI. In Section 5, we take a step to analyse the inter-parameter issues by a series of cross-comparisons on the descent directions from different gradients. Finally, we draw a brief discussion on the sensitivity analysis of the poroelastic parameters in the conclusion part. All the wavefields are solved by the fourth-order finite-difference (FD) method. Since the observed data for fluid components can not be obtained separately, the fluid adjoint source is not estimated for PFWI.

2 METHODOLOGY

2.1 Fluid-saturated poroelastic equations

Following the steps of Biot's theory (Biot 1956a, b; Biot & Willis 1957), the macroscopic equations of motion (1–2) can describe the saturated solid-fluid system across the seismic band of frequencies. Within the Biot's characteristic frequency, the fluid flow regime is treated as Poiseuille type, where the internal drag forces on the solid/fluid interface are negligible.

$$\rho \dot{v}_i + \rho_f \dot{w}_i = \partial_j \sigma_{ij}, \tag{1}$$

$$\rho_f \dot{v}_i + m \dot{w}_i = -\partial_i P - \frac{\eta}{\kappa_0} w_i. \tag{2}$$

The dots above variables denote the time differentiation and Einstein notation is applied in the equations. v_i is the solid particle velocity, and $w_i = \phi(v_i^f - v_i)$ is the Darcy filtration velocity. ϕ is the effective porosity of the porous medium and v^f is the fluid velocity. The mass coupling coefficient $m = T\rho_f/\phi$, where the tortuosity $T > 1$ is a dimensionless parameter concerns pore geometry (Ghanbarian *et al.* 2013). The average density $\rho = (1 - \phi)\rho_s + \phi\rho_f$ is comprised of the fluid density ρ_f and the solid particle density ρ_s. η denotes the fluid viscosity and κ_0 is the hydrological permeability. The stress tensor σ_{ij} and fluid pressure P are formatted by using Biot constitutive eqs (3) and (4)

$$\sigma_{ij} = c_{ijkl}\epsilon_{kl} - \alpha P \delta_{ij} + s_i, \tag{3}$$

$$-\dot{P} = M(\alpha \partial_i v_i + \partial_i w_i) + s^f, \tag{4}$$

where the Biot–Wills coefficient

$$\alpha = 1 - \frac{K_d}{K_s}, \tag{5}$$

and the fluid storage coefficient

$$M = \left(\frac{\phi}{K_f} + \frac{\alpha - \phi}{K_s}\right)^{-1}, \tag{6}$$

where c_{ijkl} is the stiffness tensor and the strain

$$\dot{\epsilon}_{ij} = \frac{1}{2}(\partial_j v_i + \partial_i v_j). \tag{7}$$

Here, $i, j, k, l \in [1, 3]$, $K_d = \lambda_d + 2/3\mu_d$, K_s and K_f represent the bulk modulus of the drained frame, solid and fluid, respectively. λ_d and μ_d are the drained Lamé parameters. (For simplification, they are not mentioned specifically and represented by λ and μ respectively in the following parts.) δ_{ij} is the Kronecker delta. The external sources s_i and s^f can be distributed in several ways: that is, only a source in the solid phase while $s^f = 0$; the source is distributed between the solid and fluid phase (Carcione *et al.* 2010). At the macroscopic scale, here, the viscosity of the fluid and attenuation mechanism are not considered during FWI under the quasi-static condition.

2.2 Boundary conditions on the free surface

At the boundary of the air-earth, the surface is free from external stress (Aki & Richards 1980). Generally, the shallow subsurface mainly consists of unconsolidated materials. Under this previous circumstance, the porous frame is drained and the pores in the porous medium are connected with the air on the traction-free surface. In the absence of dissipation ($\eta = 0$), the boundary condition on the free surface can be generalized by eqs (8) and (9) (Deresiewicz 1960)

$$\sigma_{ij} = 0, \qquad (i = \{1, 2, 3\} \equiv \{x, y, z\},\ j = 3 \equiv z), \tag{8}$$

$$P = 0. \tag{9}$$

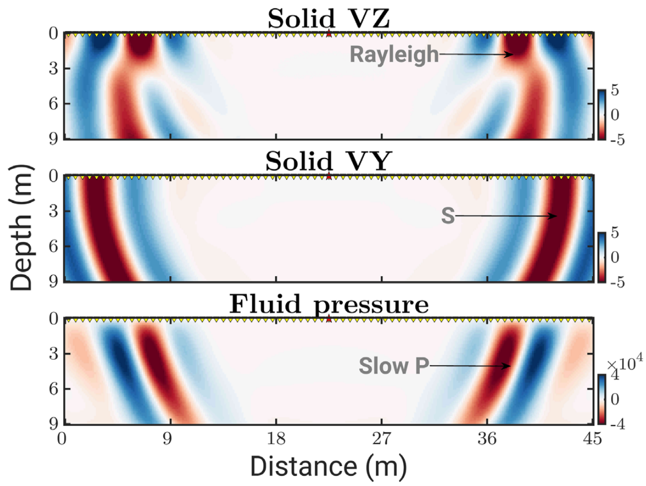

Figure 1. Snapshots of the shallow-seismic poroelastic *P-SV*&*SH* wavefields at 90 ms: triggered by Ricker wavelet with a centre frequency of 40 Hz. The model parameters are listed in Table 1.

Table 1. Rock properties of the fluid-saturated porous subsurface.

	Parameter	Symbol	Unit	Value
Grain	Bulk modulus	K_s	Pa	0.7×10^{10}
	Density	ρ_s	$kg\,m^{-3}$	2650
Matrix	Bulk modulus	K_d	Pa	5.1×10^8
	Shear modulus	μ	Pa	3.45×10^8
	Porosity	ϕ	/	0.2
	Tortuosity	T	/	2
Fluid	Bulk modulus	K_f	Pa	2.2×10^9
	Density	ρ_f	$kg\,m^{-3}$	1000
	Viscosity	η	$N{\cdot}s\,m^{-2}$	0
Velocity	Fast-*P* wave	V_{fp}	$m\,s^{-1}$	1562.23
	Slow-*P* wave	V_{sp}	$m\,s^{-1}$	303.17
	Shear wave	V_s	$m\,s^{-1}$	394.21

Fig. 1 shows the wavefields of the shallow poroelastic subsurface by solving the eqs (1)–(9) with FDTD method. As the solid vertical sources on the free surface, the triggered signal is Ricker wavelet with the centre frequency of 40 Hz. Typically, there are three types of waves: the fast compressional wave, slow compressional wave and shear wave in the poroelastic wavefields. Surface waves are involved in the shallow subsurface, such as Rayleigh wave in the *P-SV* scheme, and Love wave exists in the *SH* case, while the subsurface is inhomogeneous. From the perspective of fluid pressure, the shear waves have vanished. The fast-*P* wave can not be observed easily in the shallow poroelastic wavefields as its rapid propagation compared to other wave types. Although the slow-*P* wave is usually attenuated since the seismic band of the triggered source is normally below the Biot relaxation frequency (Johnson *et al.* 1987), here, we only consider a non-dissipation condition without the fluid viscosity ($\eta = 0$) as the surface waves will occupy most energies in the wavefields. It is shown in Fig. 1 that the velocities of the slow-*P* and *S* waves could be relatively closed under non-dissipation condition.

3 SINGLE-SCATTERING PROBLEM

The subsurface materials can be decomposed into the background medium and the perturbations. The scattered wavefields generated by small diffractors can give direct insight into the sensitivity of different parameters (Wu & Aki 1989). Although the wave front shapes of the scattered wavefields can be described by the radiation patterns, which build a connection between the incident and scattering angles (Operto *et al.* 2013; Yang *et al.* 2018), the radiation patterns of surface waves also depend on the source depth and frequencies, which makes difficulties on the analytical derivation of the radiation patterns concerns surface waves (Ben-Menahem & Harkrider 1964). Alternatively, the scattered wavefields from diffractor points concerned with various model parameters are derived explicitly and numerically visualized from a certain incident angle.

From the equations of motion and constitutive law for the fluid-saturated porous media (1)–(4), the reference model $\mathbf{m_0}$ is represented by several individual parameters (10) and the background fields $\mathbf{u_0}$ (12) consist of solid phase $\mathbf{u_s}$ and fluid phase $\mathbf{u_f}$, which is excluded in the *SH* equations.

$$\mathbf{m_0}^{P-SV} = \{\lambda, \mu, \rho_s, \rho_f, K_s, K_f, \phi\}, \tag{10}$$

$$\mathbf{m_0}^{SH} = \{\mu, \rho_s, \rho_f, \phi\}, \tag{11}$$

$$\mathbf{u_0}^{P-SV} = \{\mathbf{u_s}, \mathbf{u_f}\}, \tag{12}$$

$$\mathbf{u_0}^{SH} = \left\{\mathbf{u_s}^{SH}\right\}, \tag{13}$$

$$f : \mathbf{m} = \mathbf{m_0} + \delta\mathbf{m} \rightarrow \mathbf{u} = \mathbf{u_0} + \delta\mathbf{u}, \tag{14}$$

here f maps an element of model space $\mathbf{m}$ to the element of data space $\mathbf{u}$. Using the Born approximation, the total fields $\mathbf{u}$ can be decomposed into the primary fields $\mathbf{u_0}$ and scattered fields $\delta\mathbf{u}$ linearly.

$$f(\mathbf{u}, \mathbf{m}) = \mathbf{L}\mathbf{u} - \mathbf{s} = 0, \tag{15}$$

$$\mathbf{L}^{P-SV} = \mathbf{A} + \mathbf{B} + \mathbf{C}, \tag{16}$$

$$\mathbf{L}^{SH} = \mathbf{M} + \mathbf{N} + \mathbf{P}, \tag{17}$$

$$\mathbf{u}^{P-SV} = (v_x, v_x^f, v_z, v_z^f, \sigma_{xx}, \sigma_{zz}, \sigma_{xz}, P)^{\mathrm{T}}, \tag{18}$$

$$\mathbf{u}^{SH} = (v_y, \sigma_{xy}, \sigma_{zy})^{\mathrm{T}}, \tag{19}$$

$$\mathbf{s}^{P-SV} = (s_x, s_x^f, s_z, s_z^f, s_{xx}, s_{zz}, s_{xz}, s_p)^{\mathrm{T}}, \tag{20}$$

$$\mathbf{s}^{SH} = (s_y, s_{xy}, s_{zy})^{\mathrm{T}}, \tag{21}$$

where the forward operator $f(\mathbf{u}; \mathbf{m})$ maps the relations between the poroelastic seismic wavefields $\mathbf{u}$ and the model parameter $\mathbf{m}$. When we only consider the isotropic medium, the differential operator $\mathbf{L}$ in *P-SV* format is given by eqs (22)–(26). $\mathbf{L}^{SH}$ represents the differential operator in *SH* format, which is complemented by eq. (27).

$$\mathbf{A} = \begin{bmatrix} \mathbf{0}_4 & \mathbf{D}^1 \\ \mathbf{D}^2 & \mathbf{0}_4 \end{bmatrix} \partial_x, \tag{22}$$

$$\mathbf{D}^1 = \begin{bmatrix} -A\phi m & 0 & 0 & -A\rho_2 \\ A(\rho_f - \phi m) & 0 & 0 & A\rho_1 \\ 0 & 0 & -A\phi m & 0 \\ 0 & 0 & A(\rho_f - \phi m) & 0 \end{bmatrix}, \quad \mathbf{D}^2 = \begin{bmatrix} -(\lambda + 2\mu) & 0 & 0 & 0 \\ -\lambda & 0 & 0 & 0 \\ 0 & 0 & -\mu & 0 \\ M(\alpha - \phi) & M\phi & 0 & 0 \end{bmatrix}, \tag{23}$$

$$\mathbf{B} = \begin{bmatrix} \mathbf{0}_4 & \mathbf{D}^3 \\ \mathbf{D}^4 & \mathbf{0}_4 \end{bmatrix} \partial_z, \tag{24}$$

$$\mathbf{D}^3 = \begin{bmatrix} 0 & 0 & -A\phi m & 0 \\ 0 & 0 & A(\rho_f - \phi m) & 0 \\ 0 & -A\phi m & 0 & -A\rho_2 \\ 0 & A(\rho_f - \phi m) & 0 & A\rho_1 \end{bmatrix}, \quad \mathbf{D}^4 = \begin{bmatrix} 0 & 0 & -\lambda & 0 \\ 0 & 0 & -(\lambda + 2\mu) & 0 \\ -\mu & 0 & 0 & 0 \\ 0 & 0 & M(\alpha - \phi) & M\phi \end{bmatrix}, \tag{25}$$

$$\mathbf{C} = \begin{bmatrix} \mathbf{I}_4 & \mathbf{0}_4 \\ \mathbf{0}_4 & \mathbf{D} \end{bmatrix} \partial_t, \quad \mathbf{D} = \begin{bmatrix} 1 & 0 & 0 & \alpha \\ 0 & 1 & 0 & \alpha \\ 0 & 0 & 1 & 0 \\ 0 & 0 & 0 & 1 \end{bmatrix}, \tag{26}$$

$$\mathbf{M} = \begin{bmatrix} 0 & -A\phi m & 0 \\ -\mu & 0 & 0 \\ 0 & 0 & 0 \end{bmatrix} \partial_x, \quad \mathbf{N} = \begin{bmatrix} 0 & 0 & -A\phi m \\ 0 & 0 & 0 \\ -\mu & 0 & 0 \end{bmatrix} \partial_z, \quad \mathbf{P} = \mathbf{I}_3 \partial_t, \tag{27}$$

where $A = 1/(\rho_f(\rho T - \phi\rho_f))$. $\rho_1 = (1 - \phi)\rho_s$ and $\rho_2 = \phi\rho_f$ are the mass per unit volume of aggregate for the solid phase and the fluid phase, respectively. When the porosity $\phi = 0$, the forward operator f is able to map the elastic wavefields. The symbol $\mathbf{0}_n$ represents the $n \times n$ zero matrix, while $\mathbf{I}_n$ is the identity matrix.

Suppose that a corresponding first-order perturbation is applied on a random parameter of the reference model $\mathbf{m}_0$, the scattered wavefields δu perturbated by single parameter are obtained by eqs (28)–(30) under the Born approximation (Appendix A). For example, if there is a small scattered variable $\delta\lambda$ added on the reference parameter λ, the corresponding excitation of the scattered wavefields can be summarized as eq. (31),

$$\mathbf{L}\delta\mathbf{u}_m = \delta\mathbf{m}\delta\mathbf{s}_m, \tag{28}$$

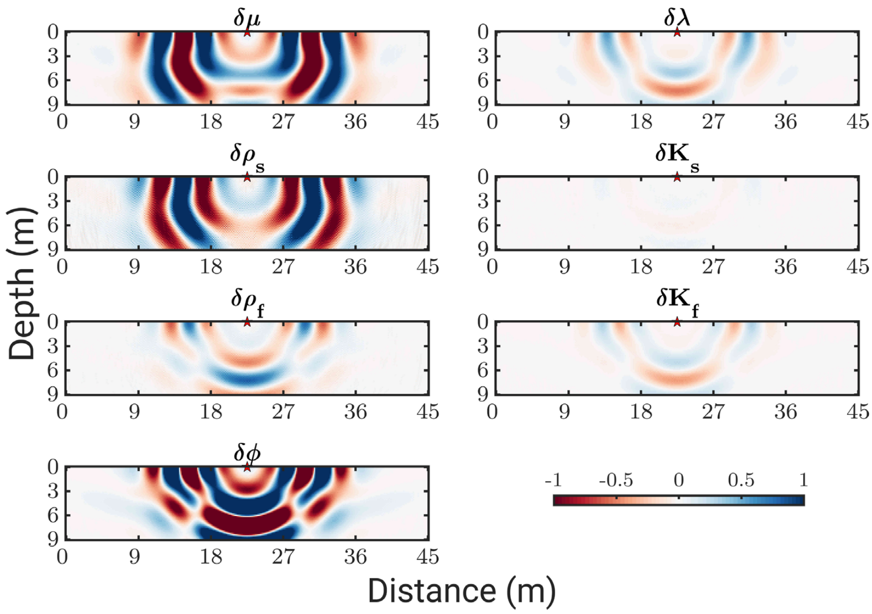

Figure 2. Shallow-seismic scattered *P-SV* poroelastic wavefields (solid profile in vertical direction *Z*) corresponding to different model parameters with 5 percent perturbations. The red star represents the location of the point diffractor.

$$\delta\mathbf{m}^{P-SV} \in \{\delta\lambda, \delta\mu, \delta\rho_s, \delta\rho_f, \delta K_s, \delta K_f, \delta\phi\}, \quad \delta\mathbf{m}^{SH} \in \{\delta\mu, \delta\rho_s, \delta\rho_f, \delta\phi\}, \tag{29}$$

$$\delta\mathbf{s}_m^{P-SV} \in \{\delta\mathbf{s}_\lambda, \delta\mathbf{s}_\mu, \delta\mathbf{s}_{\rho_s}, \delta\mathbf{s}_{\rho_f}, \delta\mathbf{s}_{K_s}, \delta\mathbf{s}_{K_f}, \delta\mathbf{s}_\phi\}, \quad \delta\mathbf{s}_m^{SH} \in \left\{\delta\mathbf{s}_\mu^{SH}, \delta\mathbf{s}_{\rho_s}^{SH}, \delta\mathbf{s}_{\rho_f}^{SH}, \delta\mathbf{s}_\phi^{SH}\right\}, \tag{30}$$

$$\delta\mathbf{s}_\lambda = \underbrace{\begin{bmatrix} \partial_x & 0 & \partial_z & 0 & \cdots & 0 & \frac{1}{K_s}\partial_t \\ \partial_x & 0 & \partial_z & 0 & \cdots & 0 & \frac{1}{K_s}\partial_t \\ 0 & & & \cdots & & & 0 \\ \frac{M}{K_s}\partial_x & 0 & \frac{M}{K_s}\partial_z & 0 & \cdots & 0 & \frac{M}{K_s^2}\partial_t \end{bmatrix}}_{(8\times 8)} \mathbf{u_0}^{P-SV}. \tag{31}$$

For instance, it shows clearly in eq. (31) that the signal of the scattering point can be calculated based on the unperturbed wavefields. The scattered wavefields are generated from the same forward operator **L** and solved by the FDTD method afterward. To be noted, since the scattering source signals are changed with various perturbed parameters, the scattering wavefields for different parameters are obtained separately.

3.1 Analysis of scattered wavefield produced by individual model parameter perturbations

In this part, a series of scattering tests are implemented on a 45 m × 9 m poroelastic half-space to detect the effects of the model parameters on the different wave types. The explicit expressions of the scattering point corresponding to various model parameters are shown in Appendix A. By solving eqs (10)–(30) with the FDTD method, both the incident and scattered wavefields are simulated numerically. A Ricker wavelet triggers the unperturbed shallow poroelastic subsurface with a centre frequency of 40 Hz on the free surface, and the scattering point (eq. 30) is set in the middle on the free surface. Model parameters can be found in Table 1.

Here we take the wave information from the solid phase as examples. The scattered wavefields corresponding to different model parameters are shown in Fig. 2 for the *P-SV* scheme and Fig. 3 for the *SH* scheme. Both for *P-SV* and *SH* cases, scattered waveform comparisons from a single trace are shown in Figs 4 and 5 separately. The number of the model parameters in the *SH* scheme is reduced since the main stress is not considered. The wave amplitude of the scattered wavefields in *P-SV* and *SH* schemes is shown consistently to make a comparison.

Different wave types in the shallow *P-SV&SH* poroelastic wavefields have been shown in Fig. 1. As shown in Fig. 3, there are only shear waves from the *SH* scheme in a homogeneous half-space, and it shows the slightest perturbation from a scattering point of the fluid density ρ_f. Shear modulus μ and solid grain density ρ_s take the main responsibility for the shear wave, while porosity has a relatively small effect. When it turns to the *P-SV* scheme in Fig. 2, Rayleigh and compressional waves are generated in the meantime. The fast-*P* wave propagates

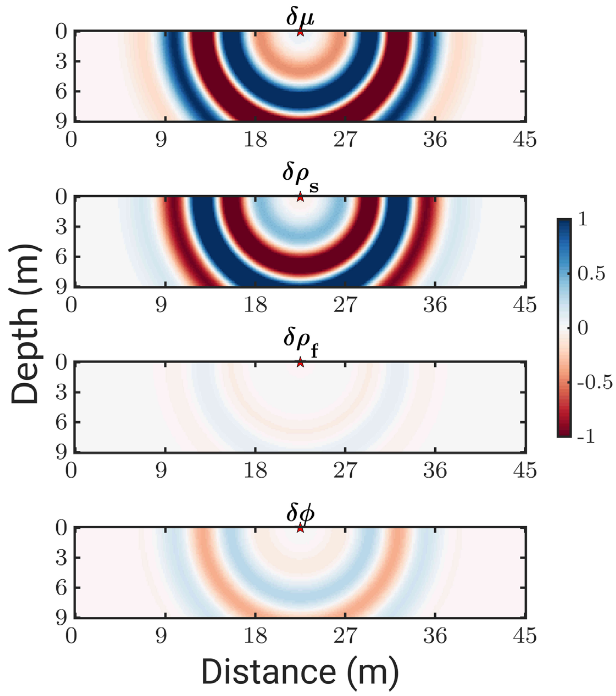

Figure 3. Shallow-seismic scattered *SH* poroelastic wavefields (Solid profile in horizontal direction *Y*) corresponding to different model parameters with 5 percent perturbations. The red star represents the location of the point diffractor, which is the same with the *P*-*SV* case.

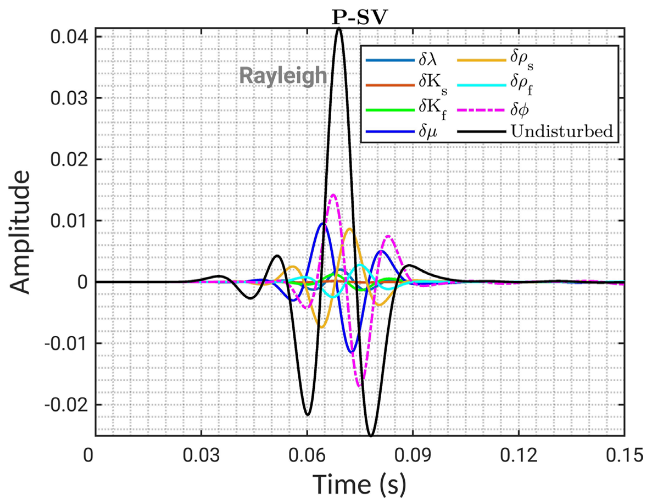

Figure 4. Scattered single-trace waveform comparison from *P*-*SV* scheme: vertical-component velocity of the solid phase. The receiver is on the free surface at offset = 10.8 m in Fig. 2, and the black line represents the unperturbed reference waveform from the homogeneous poroelastic background at the same position.

in the fastest way with relatively small energy. Besides, the velocities of the *P* and *S* waves have a significant difference since the subsurface is poroelastic, which is consistent with the scattered result from $\delta\phi$ that the porosity of the subsurface can influence body waves sensitively. Solid bulk modulus K_s shows minor effects on the shallow poroelastic wavefields. Fluid bulk modulus K_f and fluid density ρ_f take response for shear wave slightly. Furthermore, porosity ϕ is quite sensitive to both shear and compressional waves. A similar analysis also can be told from the single-trace waveform comparison in Figs 4 and 5. The results indicate the potential trade-off relations between parameters during multiparameter FWI. Based on the physical condition in the poroelastic medium, the parameters with fewer similarities in the radiation patterns are likely to be recovered together.

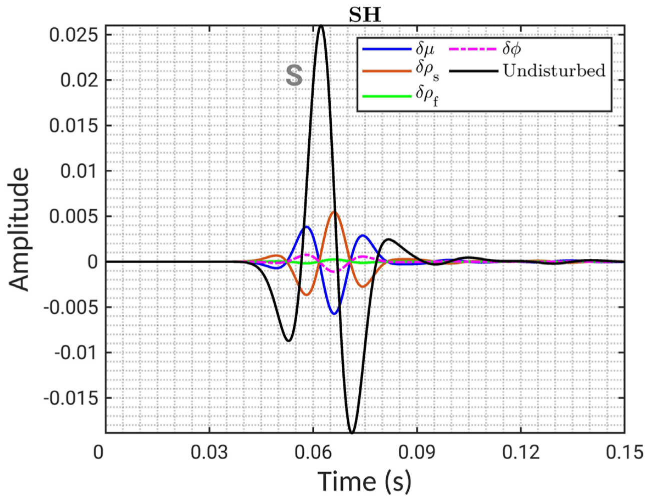

Figure 5. Scattered single-trace waveform comparison from SH scheme: horizontal-component velocity of the solid phase. The receiver is on the free surface at offset = 10.8 m in Fig. 3, and the black line represents the unperturbed reference waveform from the homogeneous poroelastic background at the same position.

4 FULL-WAVEFORM INVERSION FOR FLUID-SATURATED POROELASTIC MEDIA

The elements in the model space $\mathcal{M}$: $\mathbf{m}$ and data space $\mathcal{U}$: $\mathbf{u}$ can be decomposed as in Section 3. FWI tries to minimize the misfit functional $\mathcal{J}$, which is normally designed in a simple least-squares format (eq. 32)

$$\mathcal{J}(\mathbf{m}) = \frac{1}{2}\|\mathbf{u}(\mathbf{m}) - \mathbf{d}_{\text{obs}}\|^2 = \frac{1}{2}\sum_{\text{sources}}\int_0^T dt \sum_{r=1}^{N} \|\mathbf{u}(\mathbf{x}_\mathbf{r}, t) - \mathbf{d}_{\text{obs}}(\mathbf{x}_\mathbf{r}, t)\|^2. \tag{32}$$

T is the recording time and N indicates the number of receivers at the receiver position $\mathbf{r}$, $\mathbf{u}$ is the synthetic data and $\mathbf{d}_{\text{obs}}$ is the recorded data. To solve the minimization problem, the adjoint-state method was developed in order to avoid massive computing on the high order Fréchet derivatives (Chavent 1974; Plessix 2006).

From the perspective of Born approximation, when a perturbation $\delta\mathbf{m}$ is introduced into the reference model $\mathbf{m_0}$, the Fréchet derivative of the misfit functional is

$$\frac{\partial \mathcal{J}(\mathbf{m})}{\partial \mathbf{m}} = \sum_{\text{sources}}\int_0^T dt \sum_{r=1}^{N} \frac{\partial \delta \mathbf{u}_m}{\partial \delta \mathbf{m}}(\mathbf{u}(\mathbf{x}_\mathbf{r}, t) - \mathbf{d}_{\text{obs}}(\mathbf{x}_\mathbf{r}, t)). \tag{33}$$

Assuming a differentiable function $\mathbf{u}^*$ that satisfies

$$\mathbf{L}^*\mathbf{u}^* = \mathbf{u} - \mathbf{d}_{\text{obs}}, \tag{34}$$

for example, for two column vectors $\vec{a}$ and $\vec{b}$, $\vec{a}\cdot\vec{b} = \mathbf{a}^T\mathbf{b}$, then the Fréchet derivative of the misfit functional $\mathcal{J}$ is simplified as eq. (35) based on the eq. (28).

$$\frac{\partial \mathcal{J}(m)}{\partial m} = \sum_{\text{sources}}\int_T dt (\mathbf{L}^{-1}\delta\mathbf{s}_m)^T \mathbf{L}^*\mathbf{u}^*, \tag{35}$$

while $\mathbf{L}^* = \mathbf{L}^T$ and $\mathbf{u}^*$ represent the backpropagating adjoint wavefields (see Appendix A for $\delta\mathbf{s}_m$ and Appendix B for the Fréchet kernels with respect to different parameters),

$$\frac{\partial \mathcal{J}(m)}{\partial m} = \sum_{\text{sources}}\int_T dt (\delta\mathbf{s}_m)^T \mathbf{u}^*. \tag{36}$$

Alternatively, when a dual space $\mathcal{U}^*$: $\tilde{\mathbf{u}}^*$ is added into the mapping f, the augmented functional $\mathcal{L}$ can be defined as

$$\mathcal{L}(\tilde{\mathbf{u}}, \tilde{\mathbf{u}}^*, \mathbf{m}) = h(\tilde{\mathbf{u}}, \mathbf{m}) - \langle \tilde{\mathbf{u}}^*, f(\tilde{\mathbf{u}}, \mathbf{m})\rangle_{\mathcal{U}}, \qquad (\tilde{\mathbf{u}} \in \mathcal{U}), \tag{37}$$

where $\tilde{\mathbf{u}}$ and $\tilde{\mathbf{u}}^*$ are independent of $\mathbf{m}$ (Plessix 2006), under the physical constraint in eq. (15),

$$\mathcal{L}(\mathbf{u}, \tilde{\mathbf{u}}^*, \mathbf{m}) = h(\mathbf{u}, \mathbf{m}) - \langle \tilde{\mathbf{u}}^*, f(\mathbf{u}, \mathbf{m})\rangle_{\mathcal{U}} = \mathcal{J}(\mathbf{m}), \tag{38}$$

or

$$\mathcal{L}(\mathbf{u}, \mathbf{u}^*, \mathbf{m}) = h(\mathbf{u}, \mathbf{m}) - \langle \mathbf{u}^*, f(\mathbf{u}, \mathbf{m})\rangle_{\mathcal{U}} = \mathcal{J}(\mathbf{m}), \tag{39}$$

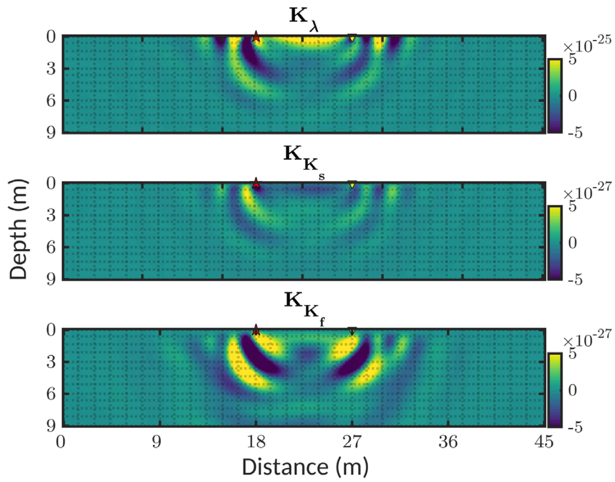

Figure 6. Fréchet kernels involving Rayleigh waves in *P-SV* for λ, K_s and K_f: The red star is the location of the forward source, and the inverted triangle represents the adjoint source. Both are located on the free surface.

for instance, the Lagrange multiplier for *P-SV* formulations

$$\mathbf{u}^* = (v_x^*, v_x^{f*}, v_z^*, v_z^{f*}, \sigma_{xx}^*, \sigma_{zz}^*, \sigma_{xz}^*, P^*)^{\mathrm{T}}, \qquad (\mathbf{u}^* \in \mathcal{U}^*), \tag{40}$$

and $(\mathbf{u}, \mathbf{u}^*)$ is the saddle point of $\mathcal{L}$. From the integration by parts, in the physical spatial domain Ω within the time duration [0, *T*], we have

$$\langle \mathbf{u}^*, \partial_t \mathbf{u}\rangle_T = -\langle \partial_t \mathbf{u}^*, \mathbf{u}\rangle_T, \tag{41}$$

and

$$\langle \mathbf{u}^*, \partial_i \mathbf{u}\rangle_\Omega = -\langle \partial_i \mathbf{u}^*, \mathbf{u}\rangle_\Omega, \qquad (i = \{1, 2, 3\} \equiv \{x, y, z\}), \tag{42}$$

when $\mathbf{u}^* = 0$ as the final time condition and the physical boundary conditions are applied as well, then the adjoint equations are generalized by

$$\frac{\partial \mathcal{L}(\mathbf{u}, \mathbf{u}^*, \mathbf{m})}{\partial \tilde{\mathbf{u}}} = \frac{\partial \mathcal{J}(\mathbf{m})}{\partial \tilde{\mathbf{u}}} - \mathbf{L}^* \mathbf{u}^* = 0. \tag{43}$$

After expanding the residual function $\mathcal{J}$ near a starting point, the model update

$$\Delta \mathbf{m} = -\gamma \mathbf{H}^{-1} \frac{\partial \mathcal{J}(\mathbf{m})}{\partial \mathbf{m}}, \tag{44}$$

which is used to approximate the real model iteratively during FWI. Here γ is the step length and $\mathbf{H}$ is the Hessian matrix. The problem of the singularity of Hessian is dealt with by approximating the inverse of Hessian with different optimization methods (Nocedal & Wright 2006).

4.1 Sensitivity kernels

The effects of different model parameters on the waveforms are evaluated from the analysis of the scattering problem in Section 3.1. As complements, the sensitivity of the various model parameters to the data space can be detected from the corresponding sensitivity kernels, which are the hearts of the related gradients as well. The full expressions of different kernels derived from the eqs (32)–(43) are in Appendix B. To clarify the effects of various wave types on the model parameters, the primary sensitivity kernels in a shallow poroelastic subsurface are calculated both in *P-SV* and *SH* equations. The numerical model is a homogeneous poroelastic half-space, with a circular anomaly within the Fresnel zone. For concerns on shallow detection, surface waves are considered. The acquisition geometry is set as the same as Section 3 within the duration time of 15 ms, and the parameters can be found in Table 1.

The kernels' galleries in Figs 6 and 7 show the wave paths for different scattering bodies. The updates along the ray path give contributes to the background values and source frequencies heavily affect the minor radius of the first-Fresnel zone. Unlike the traditional reflected wave exploration which concerns more reflections beyond the ray path, surface waves will travel along the free surface and the long wavelength parts on the fast *P* wave are less involved for shallow seismic detection. According to the wavelength Λ, here, the sequences of main wave types are $\Lambda_s > \Lambda_{\mathrm{Love}} > \Lambda_{\mathrm{Rayleigh}}$, and $\Lambda_s > \Lambda_{sp}$. Fig. 6 shows the galleries of the sensitivity kernels for λ, K_s and K_f, which are only considered in *P-SV* case. It indicates λ concerns more on the Rayleigh waves compared to K_s and K_f, while K_s and K_f are more sensitive to the compressional waves. Especially, K_s mainly gets benefits from the long wavelength components, which gives less contribution to the shallow seismic wavefields. K_f mainly concerns the slow-*P* wave, which will be attenuated in a viscous porous media within the seismic band.

Fig. 7 contains the sensitivity kernels of μ, ρ_s, ρ_f and ϕ in *P-SV* and *SH* profiles. The galleries of the same parameter are shown consistently for comparison. Compared to ρ_f and ϕ, it is clear in *SH* that μ and ρ_s are more sensitive to the shear wave components and the

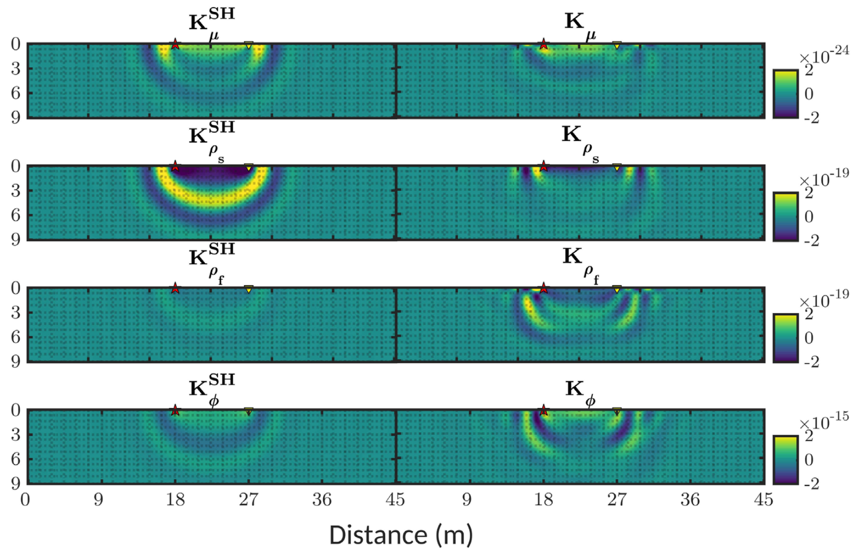

Figure 7. Fréhet kernels in *SH* & *P-SV* for μ, ρ_s, ρ_f and ϕ: surface waves are involved. Geometry is the same as in Fig. 6.

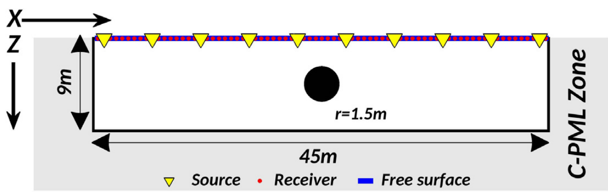

Figure 8. Acquisition geometry for a shallow poroelastic inclusion model. Horizontal *Y* component for *SH* equations is considered as well.

main energy of K_μ^{SH} distribute along the free surface. ρ_f shows less effects from shear wave components, but K_{ρ_f} indicates ρ_f is sensitive to the slow-*P* wave modes. Similarly, K_ϕ^{SH} and K_ϕ tell that ϕ takes response for shear waves but is also sensitive to *P* waves, especially the slow-*P* wave. Since Rayleigh waves are coupled from compressional waves and shear waves in *P-SV* profile, ϕ also makes substantial contributions to surface waves.

4.2 Synthetic examples of P-SV&SH PFWI for a shallow inclusion model

In this section, we perform reconstruction tests on a poroelastic inclusion model to validate the derived gradients (Appendix B) and give a preliminary insight on the feasibility of PFWI for shallow seismic data. The inclusion model consists of poroelastic background media and a circle porous anomaly in the centre. There are 10 sources and 75 receivers on the free surface. The forward wavefields are generated by Ricker wavelet with the central frequency of 40 Hz in 0.12 s. The initial model parameters come from Table 1, and Fig. 8 shows the acquisition geometry. A multistage strategy (10–20–40 Hz) is applied to avoid the cycle-skipping artifacts and a pre-conditioned steepest descent method is adopted over the course of iterations. We aim to recover anomalies of every single parameter while keeping others remain the same as the initial model, which is a homogeneous poroelastic background.

Figs 9 and 10 show a 1-D reconstruct model comparison from the middle log profile. On the basis of the derived kernels, the poroelastic parameters are well recovered by *P-SV*/Rayleigh- and *SH*/Love-wave PFWI. In Fig. 9, K_s and K_f exhibit an over-fitting problem since they are more sensitive to the long wavelength component, which makes less contribution to shallow seismic wavefields. Fig. 10 gives comparisons of the recovered μ, ρ_s, ρ_f and ϕ based on *P-SV* and *SH* equations. Especially, ρ_f is better inverted in the *P-SV* profile, which demonstrates ρ_f can get extra benefits from compressional waves. Correspondingly, Fig. 11 exhibits the changes of the poroelastic inclusion model with iterations, which show the convergence of the reconstructed model. In contrast with *SH*-wave data, the PFWI of Rayleigh-wave data usually needs more iterations as the complexity of wavefields.

5 TRADE-OFF ANALYSIS

To prepare an approach for the multiparameter inversion in fluid-saturated poroelastic media, the similarity of the sensitivities of the data to vary parameters needs to be investigated (Métivier *et al.* 2014). As derived in Section 4, the explicit expressions for kernels of the gradients in *P-SV* and *SH* formats are given by eqs (B1)–(B11) in Appendix B. We perform a series of numerical tests on the gradients of model parameters for the anomaly model in Fig. 8, and explore the correlations of their patterns. The acquisition and model parameters are the same as in Section 4.2. The inclusion model parameters are changed individually, and corresponding results are exhibited in Figs 12–18.

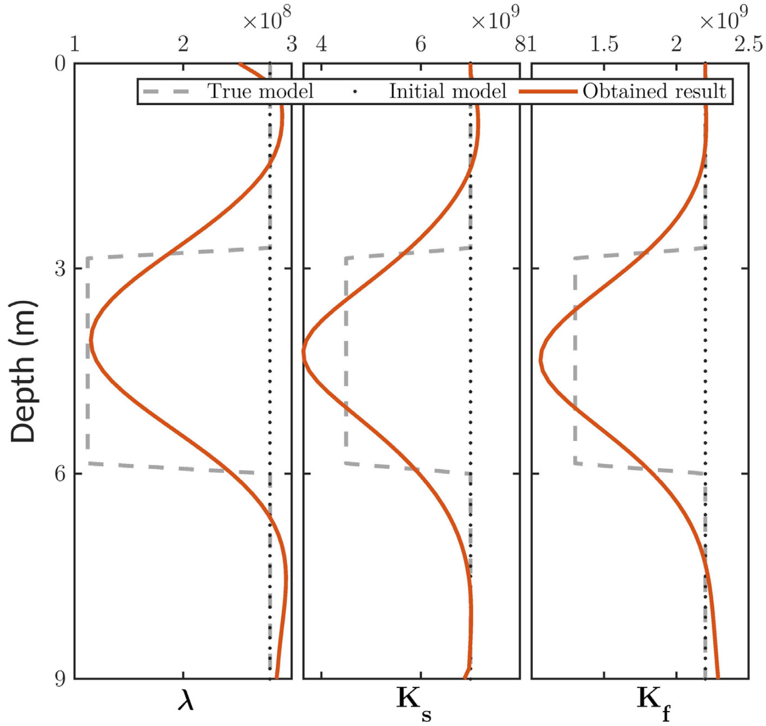

Figure 9. PFWI of Rayleigh-wave data: 1-D logging profile in the middle of the true, initial and reconstructed models for λ, K_s and K_f.

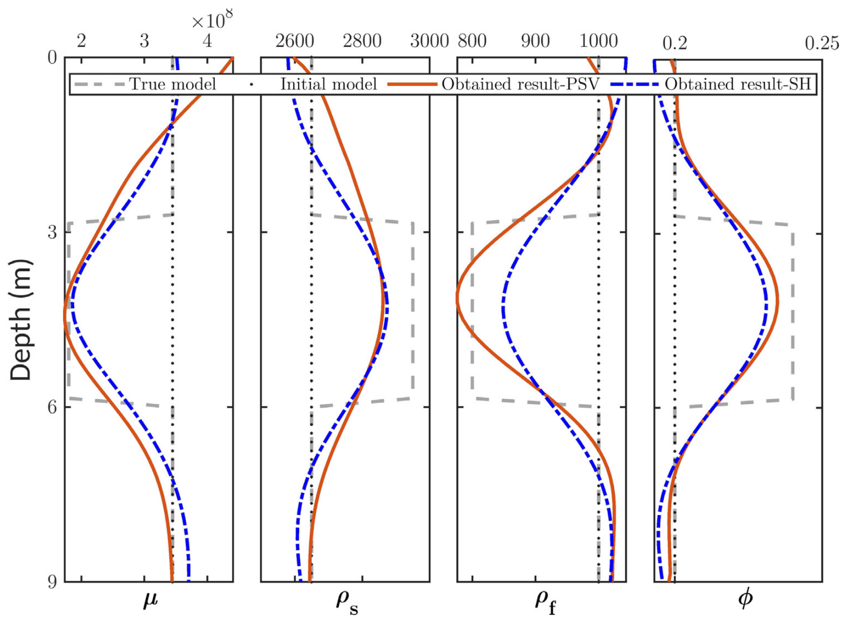

Figure 10. PFWI of *SH*/Love- and *P-SV*/Rayleigh-wave data: 1-D logging profile in the middle of the true, initial and reconstructed models for μ, ρ_s, ρ_f and ϕ.

According to the equations derived in Section 4, we know that the correlations between the gradients of different parameters can not be eliminated under the assumption of Born approximation. Because the subsurface parameters are reconstructed simultaneously during the multiparameter inversion, how to minimize the cross-talk issue and implement an applicable inversion strategy are difficult tasks. Unlike the acoustic and elastic FWI, where fewer parameters can be handled flexibly with parametrizations, we seek to divide the poroelastic parameters with low correlations into the same groups for multiparameter inversion. In this section, we vary the interference parameter of the anomaly body at the same location in the inclusion model and cross-compare the corresponding influences between the gradient patterns of other parameters. Although the values of the gradients depend on the magnitude of the related material parameters, the descent direction from the gradients panels still can indicate the correlations. Figs 12–14 only present the correlations in *P-SV*, while Figs 15–18 display the comparison results of the common parameters in *P-SV* and *SH* cases. To make clear evaluations, all the panels are scaled with their absolute maximum

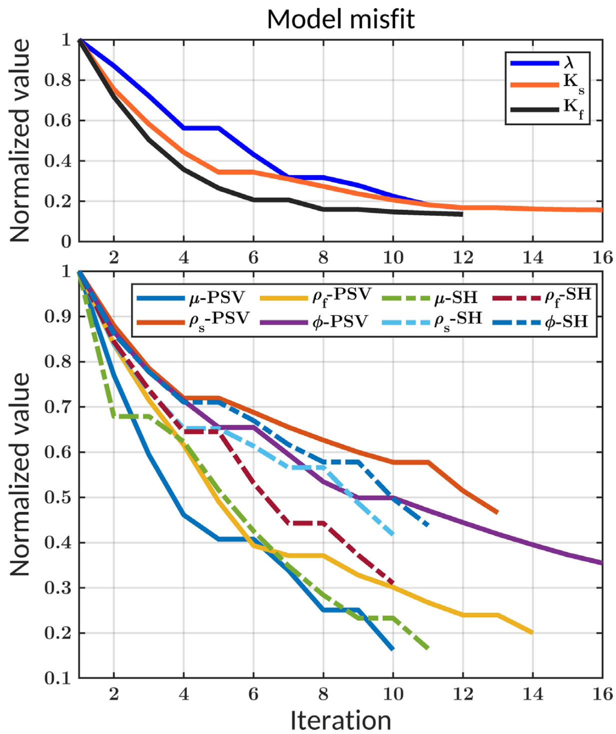

Figure 11. Model misfit changes of the poroelastic inclusion model with iterations: corresponding to the results in Figs 9 and 10.

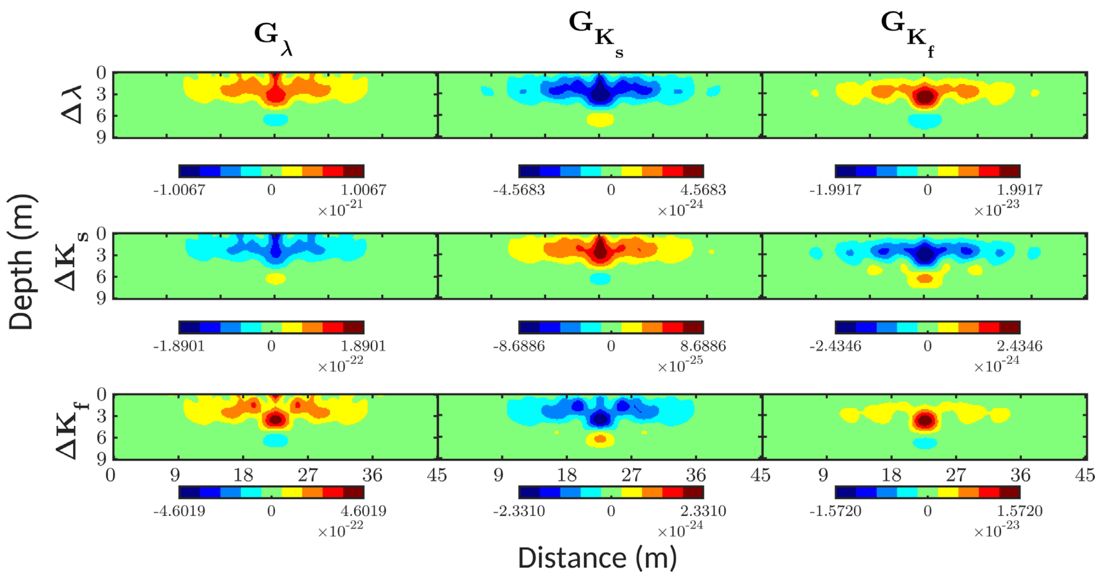

Figure 12. Gradient gallery in *P-SV* for correlation test in Section 5: $\{\Delta\lambda, \Delta K_s, \Delta K_f\} \rightarrow \{G_\lambda, G_{K_s}, G_{K_f}\}$ involving Rayleigh waves. The model geometry is shown in Fig. 8, and the parameters are listed in Table 1, which are the same as the followings.

values, which indicate the descent directions as well. To mitigate footprints from the sources and receivers, all the gradients are tapered by an error function.

The location of the absolute extreme in gradient G is likely to be closer to the surface if the related parameter has more impact on the surface waves. The key point of achieving good results by multiparameter inversion is to recover the parameters with less coherency. For example, Fig. 12 shows a map from disturbance $\{\Delta\lambda, \Delta K_s, \Delta K_f\}$ in the anomaly to the gradients $\{G_\lambda, G_{K_s}, G_{K_f}\}$ obtained from the *P-SV* poroelastic model. $\Delta\lambda \rightarrow G_{K_f}$ and $\Delta K_f \rightarrow G_\lambda$ indicate a strong coherency between λ and K_f, while the panels of $\Delta\lambda \rightarrow G_{K_s}$ and $\Delta K_s \rightarrow G_\lambda$ show fewer similarities. $\Delta K_f \rightarrow G_{K_s}$ and $\Delta K_s \rightarrow G_{K_f}$ are similar, but their descent directions are opposite. The results indicate that λ and K_s will be better to be considered in a same group during multiparameter inversion, and $\{\Delta\lambda, \Delta K_f\}$ should make changes toward the opposite direction of $\{\Delta K_s\}$ to achieve better recovery of the same anomalies.

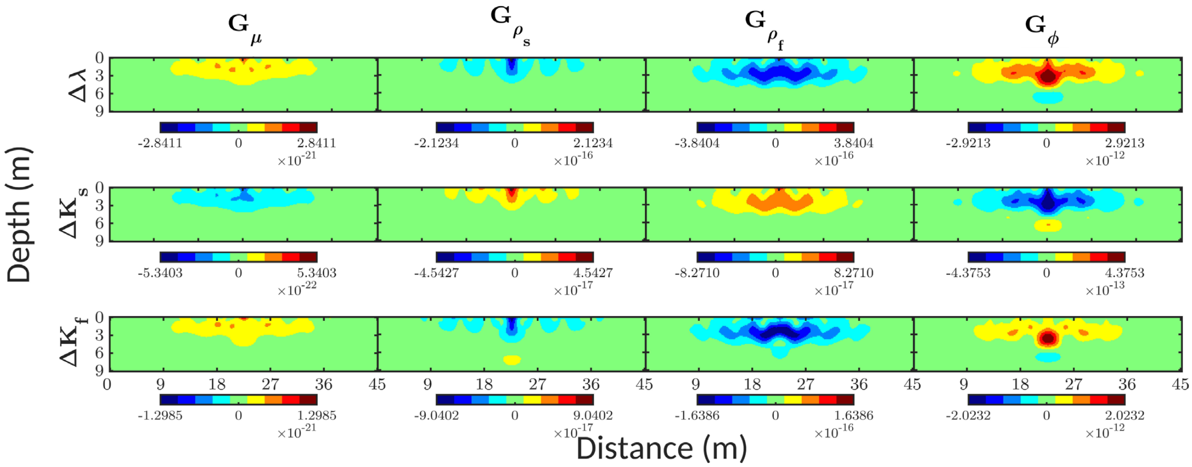

Figure 13. Gradient gallery in *P-SV* for correlation test in Section 5: $\{\Delta\lambda, \Delta K_s, \Delta K_f\} \rightarrow \{G_\mu, G_{\rho_s}, G_{\rho_f}, G_\phi\}$ involving Rayleigh waves.

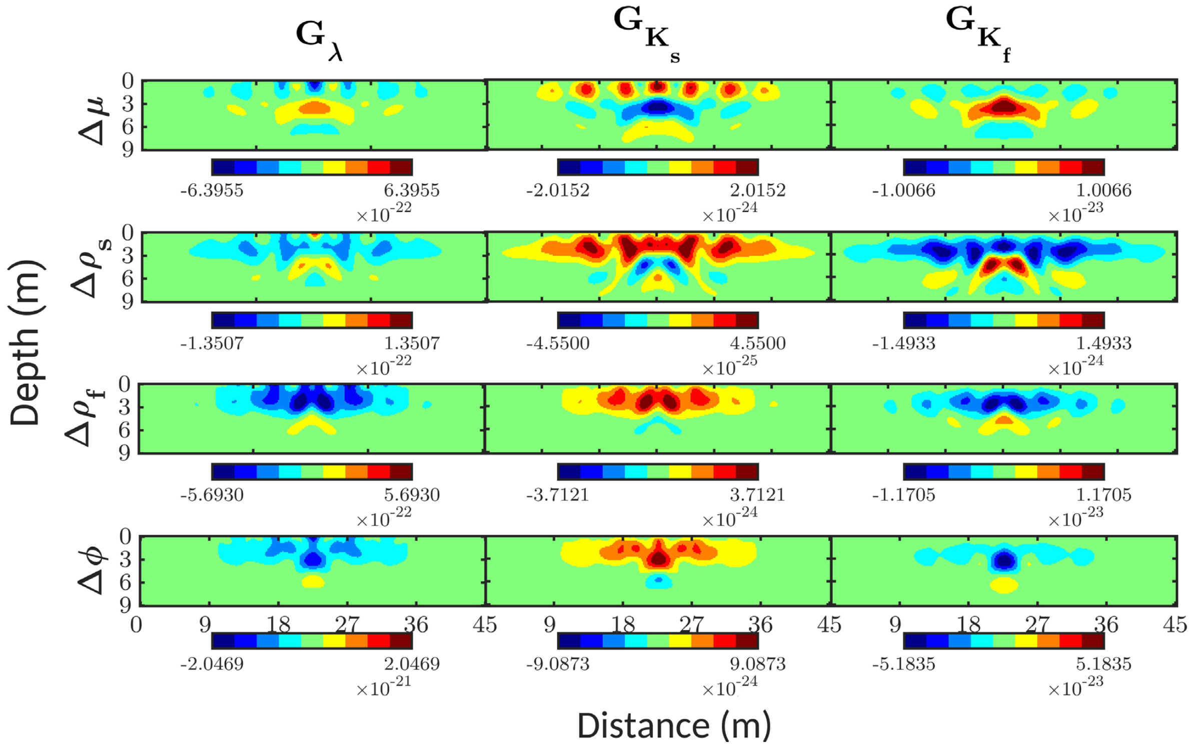

Figure 14. Gradient gallery in *P-SV* for correlation test in Section 5: $\{\Delta\mu, \Delta\rho_s, \Delta\rho_f, \Delta\phi\} \rightarrow \{G_\lambda, G_{K_s}, G_{K_f}\}$ involving Rayleigh waves.

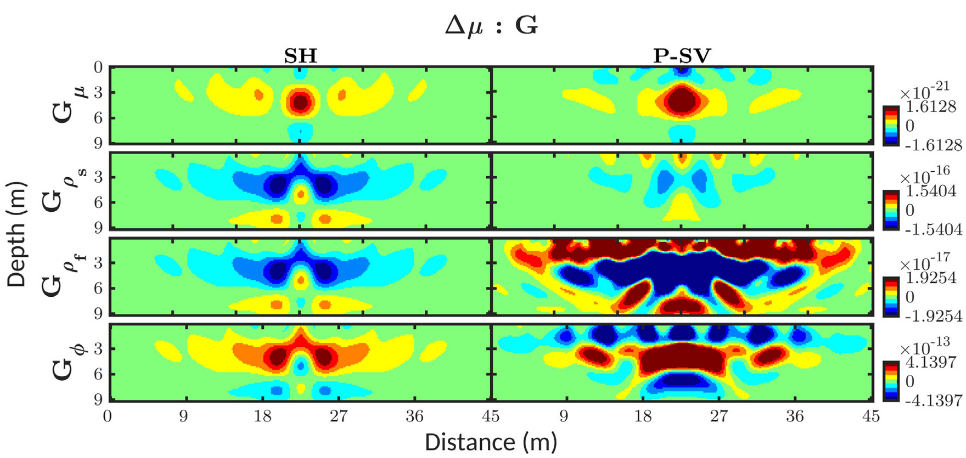

Figure 15. Gradient panel in *SH* & *P-SV* for cross-comparison: $\Delta\mu \rightarrow \{G_n, G_n^{SH}\}, n \in \{\mu, \rho_s, \rho_f, \phi\}$.

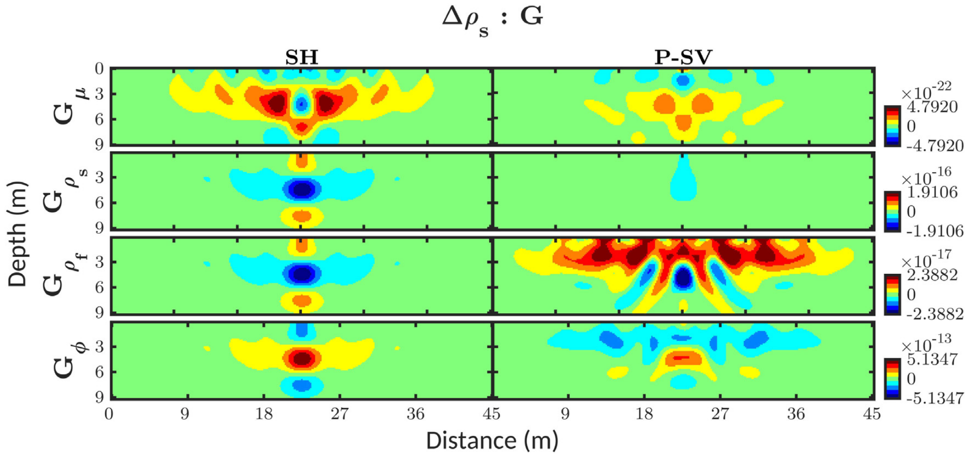

Figure 16. Gradient panel in *SH* & *P-SV* for cross-comparison: $\Delta\rho_s \rightarrow \{G_n, G_n^{SH}\}$, $n \in \{\mu, \rho_s, \rho_f, \phi\}$.

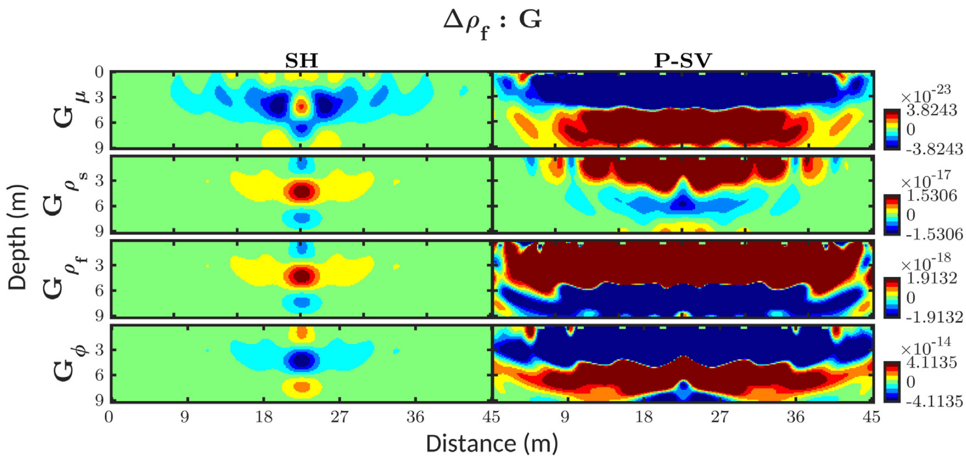

Figure 17. Gradient panel in *SH* & *P-SV* for cross-comparison: $\Delta\rho_f \rightarrow \{G_n, G_n^{SH}\}$, $n \in \{\mu, \rho_s, \rho_f, \phi\}$.

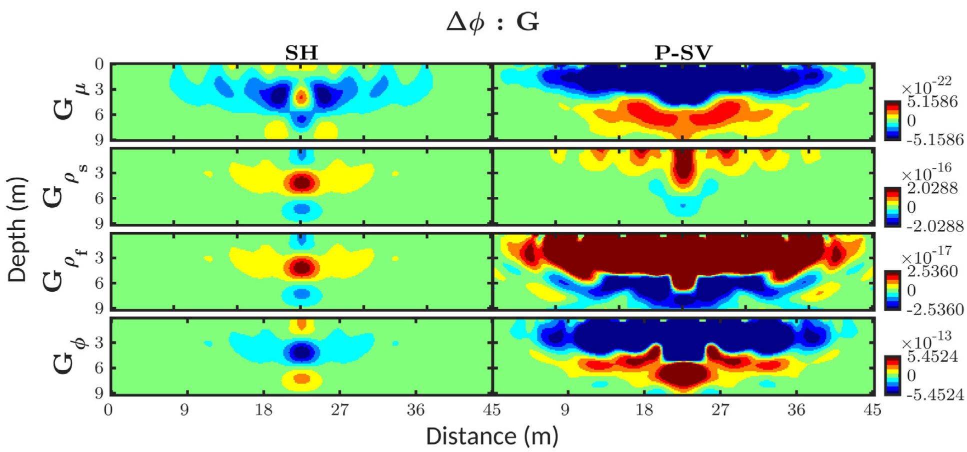

Figure 18. Gradient panel in *SH* & *P-SV* for cross-comparison: $\Delta\phi \rightarrow \{G_n, G_n^{SH}\}$, $n \in \{\mu, \rho_s, \rho_f, \phi\}$.

Figs 13 and 14 exhibit the maps $\Delta m \rightarrow G_n$, where $m \in \mathbf{M}$ and $n \in \mathbf{N}$ ($\mathbf{M}, \mathbf{N} \subseteq \{(\lambda, K_s, K_f), (\mu, \rho_s, \rho_f, \phi)\}$, $\mathbf{M} \neq \mathbf{N}$). By the cross-comparison of G_n mapped from Δm, the gradients performing without concentrated descent direction at the location of the anomaly shows fewer correlations between m and n. For instance, $\Delta m \rightarrow G_\phi$ and $\Delta\phi \rightarrow G_n$ indicate that porosity ϕ can raise cross-talk issues easily when inverted together with $m \in (\lambda, K_s, K_f)$. Besides, $\Delta\lambda \rightarrow G$ and $\Delta K_f \rightarrow G$ have similar patterns, and the result is consist with Fig. 12. Compared to ρ_f, (μ, ρ_s) have less coherency with (λ, K_s, K_f).

Figs 15–18 present the results of the cross comparison Δm: $G_n(m, n \in \{\mu, \rho_s, \rho_f, \phi\})$ in both *SH* and *P-SV* cases, while Love and Rayleigh waves exist separately. The gradient panels are shown consistently in *P-SV* and *SH*. In *SH* panels, $\Delta\mu \rightarrow G_n^{SH}(n \in \{\rho_s, \rho_f, \phi\})$ and

$\Delta m \rightarrow G_{\mu}^{SH}(m \in \{\rho_s, \rho_f, \phi\})$ illustrate that μ is a harmless and essential parameter for multiparameter PFWI. The panels of $\Delta\rho_s \rightarrow G_n(n \in \{\mu, \rho_f, \phi\})$ and $\Delta m \rightarrow G_{\rho_s}(m \in \{\mu, \rho_f, \phi\})$ show the correlations of gradients in *P-SV* are decreased compared to *SH*, which indicates it is more realistic to invert ρ_s, μ and ϕ simultaneously in *P-SV* PFWI. Besides, G_{ρ_s} and G_{ρ_f} look similar, and the descent direction of G_ϕ and (G_{ρ_s}, G_{ρ_f}) is opposite. The analysis based on Figs 12–18 can provide insights into the parametrization of multiparameter PFWI.

6 CONCLUSIONS

We present a theoretical framework for TD poroelastic FWI, especially for shallow-seismic data. The shallow-seismic *P-SV&SH* poroelastic wavefields are simulated numerically. Based upon Born approximation, we derived the single-scattering *P-S&SH* wave equations for the fluid-saturated poroelastic media. The contributions of the single poroelastic parameters (*P-SV*: λ, μ, ρ_s, ρ_f, K_s, K_f, ϕ; *SH*: μ, ρ_s, ρ_f, ϕ) on the shallow-seismic wavefields are discussed by comparing the corresponding scattered wavefields, respectively. With the help of the adjoint-state method, the explicit formulations of the sensitivity kernels for different model parameters are derived by perturbation theory and Lagrange augmented functional. The kernel galleries in *P-SV&SH* are used to further illustrate the sensitivities of the poroelastic parameters to different wave components. Besides, we implement reconstruction tests on a poroelastic inclusion model to verify the accuracy of the derived kernels, and the recovery ability of PFWI on *P-SV*/Rayleigh- and *SH*/Love-wave data is compared, respectively. As a preliminary preparation for multiparameter FWI, we have also investigated the inter-parameter issues based on the descent direction in the *P-SV&SH* panels of gradients.

Similar to the elastic FWI, the results indicate that shear modulus μ and grain density ρ_s are mainly responsible for generating shear waves. The fluid density ρ_f, which is extracted from the overall density ρ, pays primary attention to the slow-*P* wave mode. λ, which also exists in elastodynamic equations, and grain bulk modulus K_s has similar effects. In addition, fluid bulk modulus K_f and porosity ϕ mainly concern with the slow-*P* wave mode. ϕ has effects on all the wave types but prefers compressional waves. According to the real subsurface condition, it is necessary to classify the parameters with fewer correlations as a group to minimize the cross-talk issues during multiparameter PFWI. For instance, λ and K_f are not suitable to invert together in PFWI of Rayleigh-wave data. ρ_s and ρ_f can hardly be detected together in PFWI of Love-wave data, but their correlation is minimized in *P-SV* equations. Since the effective velocities of the poroelastic subsurface are coupled with different parameters (Appendix C), we can hardly obtain the updates on their gradients directly during the inversion. The feasibility and reconstructability of multiparameter TD-PFWI will be discussed in subsequent publications, especially for the fluid information.

ACKNOWLEDGMENTS

The authors would like to thank the editor Hervé Chauris and an anonymous reviewer for their constructive comments. TL acknowledges the financial support from the China Scholarship Council.

DATA AVAILABILITY

The numerical data used in this work are available on request.

REFERENCES

Aki, K. & Richards, P., 1980. *Quantitative Seismology: Theory and Methods, no. v. 1-2 in Geology Series,* W. H. Freeman.

Ben-Menahem, A. & Harkrider, D.G., 1964. Radiation patterns of seismic surface waves from buried dipolar point sources in a flat stratified earth, *J. geophys. Res.,* **69**(12), 2605–2620.

Biot, M.A., 1956a. Theory of propagation of elastic waves in a fluid-saturated porous solid. i. low-frequency range, *J. acoust. Soc. Am.,* **28**(2), 168–178.

Biot, M.A., 1956b. Theory of propagation of elastic waves in a fluid-saturated porous solid. ii. higher frequency range, *J. acoust. Soc. Am.,* **28**(2), 179–191.

Biot, M.A. & Willis, D.G., 1957. The elastic coefficients of the theory of consolidation, *J. appl. Mech.,* **24,** 594–601.

Butler, D., 2005. *Near-surface Geophysics, Investigations in geophysics Near-surface geophysics,* Society of Exploration Geophysicists.

Carcione, J.M., Morency, C. & Santos, J.E., 2010. Computational poroelasticity—a review, *Geophysics,* **75**(5), 75A229–75A243.

Chavent, G., 1974. Identification of functional parameters in partial differential equations, *Joint Autom. Contr. Conf.,* **12,** 155–156.

Dai, N., Vafidis, A. & Kanasewich, E.R., 1995. Wave propagation in heterogeneous, porous media: a velocity-stress, finite-difference method, *Geophysics,* **60**(2), 327–340.

De Barros, L., Dietrich, M. & Valette, B., 2010. Full waveform inversion of seismic waves reflected in a stratified porous medium, *J. geophys. Int.,* **182**(3), 1543–1556.

Deresiewicz, H., 1960. The effect of boundaries on wave propagation in a liquid-filled porous solid: I. Reflection of plane waves at a free plane boundary (non-dissipative case), *Bull. seism. Soc. Am.,* **50**(4), 599–607.

Dupuy, B., Garambois, S., Asnaashari, A., Balhareth, H.M., Landrø, M., Stovas, A. & Virieux, J., 2016. Estimation of rock physics properties from seismic attributes—part 2: applications, *Geophysics,* **81**(4), M55–M69.

Fichtner, A., 2010. *Full Seismic Waveform Modelling and Inversion, Advances in Geophysical and Environmental Mechanics and Mathematics,* Springer Berlin Heidelberg.

Gassmann, F., 1951. Elastic waves through a packing of spheres, *Geophysics,* **16**(4), 673–685.

Ghanbarian, B., Hunt, A.G., Ewing, R.P. & Sahimi, M., 2013. Tortuosity in porous media: A critical review, *Soil Sci. Soc. Am. J.,* **77**(5), 1461–1477.

Hu, Q., Keating, S., Innanen, K.A. & Chen, H., 2021. Direct updating of rock-physics properties using elastic full-waveform inversion, *Geophysics,* **86**(3), MR117–MR132.

Johnson, D.L., Koplik, J. & Dashen, R., 1987. Theory of dynamic permeability and tortuosity in fluid-saturated porous media, *J. Fluid Mech.,* **176,** 379–402.

Masson, Y.J., Pride, S.R. & Nihei, K.T., 2006. Finite difference modeling of biot's poroelastic equations at seismic frequencies, *J. geophys. Res.: Solid Earth,* **111**(B10), doi:10.1029/2006JB004366.

Métivier, L., Brossier, R., Operto, S. & Virieux, J., 2014. Multi-parameter FWI - an illustration of the Hessian operator role for mitigating trade-off between parameter classes, *European Association of Geoscientists & Engineers,* **2014**(1), 1–5.

Morency, C., Luo, Y. & Tromp, J., 2009. Finite-frequency kernels for wave propagation in porous media based upon adjoint methods, *J. geophys. Int.,* **179**(2), 1148–1168.

Morency, C. & Tromp, J., 2008. Spectral-element simulations of wave propagation in porous media, *J. geophys. Int.,* **175**(1), 301–345.

Nocedal, J. & Wright, S.J., 2006. *Numerical Optimization,* Springer, New York, NY, USA 2nd edn.

Operto, S., Gholami, Y., Prieux, V., Ribodetti, A., Brossier, R., Metivier, L. & Virieux, J., 2013. A guided tour of multiparameter full-waveform inversion with multicomponent data: From theory to practice, *Leading Edge,* **32**(9), 1040–1054.

Plessix, R.-E., 2006. A review of the adjoint-state method for computing the gradient of a functional with geophysical applications, *J. geophys. Int.,* **167**(2), 495–503.

Queißer, M. & Singh, S.C., 2013. Full waveform inversion in the time lapse mode applied to co2 storage at sleipner, *Geophys. Prospect.,* **61**(3), 537–555.

Tarantola, A. & Valette, B., 1982. Generalized nonlinear inverse problems solved using the least squares criterion, *Rev. Geophys.,* **20**(2), 219–232.

Virieux, J. & Operto, S., 2009. An overview of full-waveform inversion in exploration geophysics, *Geophysics,* **74**(6), WCC1–WCC26.

Wu, R. & Aki, K., 1985. Scattering characteristics of elastic waves by an elastic heterogeneity, *Geophysics,* **50**(4), 582–595.

Wu, R. & Aki, K., 1989. *Scattering and Attenuation of Seismic Waves, Part II, Pageoph Topical Volumes,* Birkhäuser Basel.

Yang, Q. & Malcolm, A., 2020. Frequency domain full-waveform inversion in a fluid-saturated poroelastic medium, *J. geophys. Int.,* **225**(1), 68–84.

Yang, Q., Malcolm, A., Rusmanugroho, H. & Mao, W., 2018. Analysis of radiation patterns for optimized full waveform inversion in fluid-saturated porous media, *J. geophys. Int.,* **216**(3), 1919–1937.

Zhu, X. & McMechan, G.A., 1991. Numerical simulation of seismic responses of poroelastic reservoirs using biot theory, *Geophysics,* **56**(3), 328–339.

APPENDIX A: FIRST-ORDER SCATTERING PULSES

The perturbated body can be treated as a point scatterer when the size of the scatterer is much smaller than the wavelength (Wu & Aki 1989). Following the eqs (10)–(14), by using Born approximation, the explicit expressions of secondary sources $\delta\mathbf{m}\delta\mathbf{s}_m$ (eqs 28–29) for the remained single perturbated parameter in the isotropic fluid-saturated porous media are given by eqs (A1)-(A6).

$$\delta\mathbf{s}_\mu = \underbrace{\begin{bmatrix} \\ \\ \\ \\ 2\partial_x & 0 & \cdots & 0 & \cdots & 0 & \frac{2}{3K_s}\partial_t \\ 0 & 0 & 2\partial_z & 0 & \cdots & 0 & \frac{2}{3K_s}\partial_t \\ \partial_z & 0 & \partial_x & 0 & \cdots & & 0 \\ \frac{2M}{3K_s}\partial_x & 0 & \frac{2M}{3K_s}\partial_z & 0 & \cdots & 0 & \frac{2M}{3K_s^2}\partial_t \end{bmatrix}}_{(8\times8)} \mathbf{u_0}^{P-SV}, \tag{A1}$$

$$\delta\mathbf{s}_{\rho_s} = -A\rho_f(1-\phi) \underbrace{\begin{bmatrix} T\partial_t & 0 & \cdots & & & 0 \\ (T-1)\partial_t & 0 & \cdots & & & 0 \\ 0 & 0 & T\partial_t & 0 & \cdots & 0 \\ 0 & 0 & (T-1)\partial_t & 0 & \cdots & 0 \\ \\ \\ \\ \\ \end{bmatrix}}_{(8\times8)} \mathbf{u_0}^{P-SV}, \tag{A2}$$

$$\delta\mathbf{s}_{\rho_f} = A \underbrace{\begin{bmatrix} -(T-1)\rho_2\partial_t & 0 & \cdots & & & & 0 \\ (T-1)\rho_1\partial_t & -\frac{1}{A\rho_f}\partial_t & 0 & \cdots & & & 0 \\ 0 & 0 & -(T-1)\rho_2\partial_t & 0 & \cdots & & 0 \\ 0 & 0 & (T-1)\rho_1\partial_t & -\frac{1}{A\rho_f}\partial_t & 0 & \cdots & 0 \\ \\ \\ \\ \\ \end{bmatrix}}_{(8\times8)} \mathbf{u_0}^{P-SV}, \tag{A3}$$

$$\delta\mathbf{s}_{K_s} = \frac{\alpha-1}{K_s} \underbrace{\begin{bmatrix} \\ \\ \\ \\ 0 & & \cdots & & 0 & \partial_t \\ 0 & & \cdots & & 0 & \partial_t \\ 0 & & & \cdots & & 0 \\ M\partial_x & 0 & M\partial_z & 0 & \cdots & 0 & M\frac{1-2\alpha+\phi}{K_s(1-\alpha)}\partial_t \end{bmatrix}}_{(8\times8)} \mathbf{u_0}^{P-SV}, \tag{A4}$$

$$\delta \mathbf{s}_{K_f} = \underbrace{\begin{bmatrix} & & & \\ & & & \\ & & & \\ 0 & \cdots & 0 & \frac{\phi M}{K_f^2}\partial_t \end{bmatrix}}_{(8\times8)} \mathbf{u_0}^{P-SV}, \tag{A5}$$

$$\delta \mathbf{s}_{\phi} = A\rho_f \underbrace{\begin{bmatrix} T\rho_s\partial_t & -T\rho_f\partial_t & 0 & \cdots & & & 0 \\ (T-1)\rho_s\partial_t & -(T-1)\rho_f\partial_t & 0 & \cdots & & & \vdots \\ 0 & 0 & T\rho_s\partial_t & -T\rho_f\partial_t & 0 & \cdots & \\ 0 & 0 & (T-1)\rho_s\partial_t & -(T-1)\rho_f\partial_t & 0 & \cdots & 0 \\ & & & & & & \\ \frac{\alpha M}{A\rho_f\phi}\partial_x & 0 & \frac{\alpha M}{A\rho_f\phi}\partial_z & 0 & \cdots & 0 & \frac{\alpha M}{A\rho_f\phi K_s}\partial_t \end{bmatrix}}_{(8\times8)} \mathbf{u_0}^{P-SV}. \tag{A6}$$

Here, $\rho_1 = (1-\phi)\rho_s$ and $\rho_2 = \phi\rho_f$ represent the mass of solid and fluid per unit volume of aggregate, respectively (Biot 1956a). Besides, the scattering sources for *SH* equations are also summarized as eqs (A7)–(A8).

$$\delta \mathbf{s}_{\mu}^{SH} = \underbrace{\begin{bmatrix} \partial_x & 0 & 0 \\ \partial_z & 0 & 0 \end{bmatrix}}_{(3\times3)} \mathbf{u_0}^{SH}, \quad \delta \mathbf{s}_{\phi}^{SH} = -A\rho_f[(T-1)\rho_f - T\rho_s] \underbrace{\begin{bmatrix} \partial_t & 0 & 0 \\ & & \\ & & \end{bmatrix}}_{(3\times3)} \mathbf{u_0}^{SH}. \tag{A7}$$

$$\delta \mathbf{s}_{\rho_s}^{SH} = -AT\rho_f(1-\phi) \underbrace{\begin{bmatrix} \partial_t & 0 & 0 \\ & & \\ & & \end{bmatrix}}_{(3\times3)} \mathbf{u_0}^{SH}, \quad \delta \mathbf{s}_{\rho_f}^{SH} = -A(T-1)\rho_2 \underbrace{\begin{bmatrix} \partial_t & 0 & 0 \\ & & \\ & & \end{bmatrix}}_{(3\times3)} \mathbf{u_0}^{SH} \tag{A8}$$

APPENDIX B: SENSITIVITY KERNELS WITH RESPECT TO INDIVIDUAL PARAMETERS

Since the Fréchet or sensitivity kernels are the volumetric densities of Fréchet derivatives (Fichtner 2010), when the unknown variables in the misfit function are the displacement differences, the explicit 2-D sensitivity kernels $\boldsymbol{K}$ in the direction $\delta\mathbf{m}$ are derived on the basis of the eq. (33). Both the *P-SV* and SH equations are considered bellow.

For elastic modulus,

$$\boldsymbol{K}_{\lambda} = -\int_0^T dt \left\{ A\rho_f \left[T\left(\frac{\partial u_x^*}{\partial x} + \frac{\partial u_z^*}{\partial z}\right) + (T-1)\left(\frac{\partial u_x^{f*}}{\partial x} + \frac{\partial u_z^{f*}}{\partial z}\right)\right] + \frac{M}{K_s}P^* \right\} \left(\frac{\partial u_x}{\partial x} + \frac{\partial u_z}{\partial z} + \frac{1}{K_s}P\right). \tag{B1}$$

For shear modulus,

$$\begin{aligned} \boldsymbol{K}_{\mu} = -\int_0^T dt \Bigg\{ & A\rho_f \Bigg[T\left[2\left(\frac{\partial u_x^*}{\partial x}\frac{\partial u_x}{\partial x} + \frac{\partial u_z^*}{\partial z}\frac{\partial u_z}{\partial z}\right) + \left(\frac{\partial u_z^*}{\partial x} + \frac{\partial u_x^*}{\partial z}\right)\left(\frac{\partial u_z}{\partial x} + \frac{\partial u_x}{\partial z}\right)\right] \\ & + (T-1)\left[2\left(\frac{\partial u_x^{f*}}{\partial x}\frac{\partial u_x}{\partial x} + \frac{\partial u_z^{f*}}{\partial z}\frac{\partial u_z}{\partial z}\right) + \left(\frac{\partial u_z^{f*}}{\partial x} + \frac{\partial u_x^{f*}}{\partial z}\right)\left(\frac{\partial u_z}{\partial x} + \frac{\partial u_x}{\partial z}\right)\right]\Bigg] \\ & + \frac{2}{3K_s}\left[\frac{1}{\alpha}P\left[A\left(\rho_2\left(\frac{\partial u_x^*}{\partial x} + \frac{\partial u_z^*}{\partial z}\right) - \rho_1\left(\frac{\partial u_x^{f*}}{\partial x} + \frac{\partial u_z^{f*}}{\partial z}\right)\right) - P^*\right] \right. \\ & \left. + MP^*\left(\frac{\partial u_x}{\partial x} + \frac{\partial u_z}{\partial z} + \frac{1}{K_s}P\right)\right]\Bigg\}, \end{aligned} \tag{B2}$$

and

$$\boldsymbol{K}_{\mu}^{SH} = -\int_0^T dt\, AT\rho_f \left(\frac{\partial u_y^*}{\partial x}\frac{\partial u_y}{\partial x} + \frac{\partial u_y^*}{\partial z}\frac{\partial u_y}{\partial z}\right). \tag{B3}$$

For solid particle density,

$$\boldsymbol{K}_{\rho_s} = -\int_0^T dt\, A\rho_f(1-\phi)\left\{\frac{\partial v_x}{\partial t}\left[Tu_x^* + (T-1)u_x^{f*}\right] + \frac{\partial v_z}{\partial t}\left[Tu_z^* + (T-1)u_z^{f*}\right]\right\}, \tag{B4}$$

and

$$\boldsymbol{K}_{\rho_s}^{SH} = -\int_0^T dt\, AT\rho_f(1-\phi)u_y^*\frac{\partial v_y}{\partial t}. \tag{B5}$$

For fluid density,

$$\boldsymbol{K}_{\rho_f} = -\int_0^T dt\left\{A(T-1)\left[\frac{\partial v_x}{\partial t}\left(\rho_2 u_x^* - \rho_1 u_x^{f*}\right) + \frac{\partial v_z}{\partial t}\left(\rho_2 u_z^* - \rho_1 u_z^{f*}\right)\right] + \frac{1}{\rho_f}\left(\frac{\partial v_x^f}{\partial t}u_x^{f*} + \frac{\partial v_z^f}{\partial t}u_z^{f*}\right)\right\}, \tag{B6}$$

and

$$\boldsymbol{K}_{\rho_f}^{SH} = -\int_0^T dt\, A(T-1)\rho_2 u_y^*\frac{\partial v_y}{\partial t}. \tag{B7}$$

For solid bulk modulus,

$$\boldsymbol{K}_{K_s} = \int_0^T dt\,\frac{1-\alpha}{K_s}\left\{A\rho_f P\left[T\left(\frac{\partial u_x^*}{\partial x} + \frac{\partial u_z^*}{\partial z}\right) + (T-1)\left(\frac{\partial u_x^{f*}}{\partial x} + \frac{\partial u_z^{f*}}{\partial z}\right)\right]\right.$$
$$\left. + MP^*\left[\frac{\partial u_x}{\partial x} + \frac{\partial u_z}{\partial z} + \frac{1-2\alpha+\phi}{K_s(1-\alpha)}P\right]\right\}. \tag{B8}$$

For fluid bulk modulus,

$$\boldsymbol{K}_{K_f} = -\int_0^T dt\,\frac{\phi M}{K_f^2}PP^*. \tag{B9}$$

For porosity,

$$\boldsymbol{K}_{\phi} = \int_0^T dt\left\{-A\rho_f\left[\left(\rho_f\frac{\partial v_x^f}{\partial t} - \rho_s\frac{\partial v_x}{\partial t}\right)\left(Tu_x^* + (T-1)\,u_x^{f*}\right) + \left(\rho_f\frac{\partial v_z^f}{\partial t} - \rho_s\frac{\partial v_z}{\partial t}\right)\left(Tu_z^* + (T-1)\,u_z^{f*}\right)\right]\right.$$
$$\left. - \frac{\alpha M}{\phi}P^*\left(\frac{\partial u_x}{\partial x} + \frac{\partial u_z}{\partial z} + \frac{1}{K_s}P\right)\right\}, \tag{B10}$$

and

$$\boldsymbol{K}_{\phi}^{SH} = -\int_0^T dt\, A\rho_f[(T-1)\rho_f - T\rho_s]u_y^*\frac{\partial v_y}{\partial t} \tag{B11}$$

Here u and u^* represent the displacement in the forward system and adjoint system, respectively. It is worth to know that the Fréchet kernels also depend on the model parametrization and the forward component applied in the calculation of the misfit function. Both the components of the fluid phase in the forward and adjoint wavefields are vanished when the porosity is equal to zero, which supplies a way to simplify the poroelastic media into an elastic and acoustic medium.

APPENDIX C: EFFECTIVE VELOCITIES

The parameters and formulations for the calculation of the velocities in the poroelastic media are summarized below (Biot & Willis 1957; Dai *et al.* 1995). The definition of the parameters has already been explained in the main text.

$$\begin{cases} P = [(1-\phi)(\alpha-\phi) + \frac{\phi K_d}{K_f}]M + \frac{4}{3}\mu \\ Q = \phi M(\alpha-\phi) \\ R = \phi^2 M \end{cases}, \tag{C1}$$

$$\begin{cases} A' = T\phi\rho\rho_f - (-\phi\rho_f)^2 \\ B' = \rho R + T\phi\rho_f P + 2\phi\rho_f Q \\ C' = PR - Q^2 \end{cases}. \tag{C2}$$

Then, the velocity of the fast compressional wave

$$V_{fp} = \sqrt{\frac{B'^2 + \sqrt{B'^2 - 4A'C'}}{2A'}}, \tag{C3}$$

the velocity of the slow compressional wave

$$V_{sp} = \sqrt{\frac{B'^2 - \sqrt{B'^2 - 4A'C'}}{2A'}}. \tag{C4}$$

The fluid viscosity is absent in the non-dissipative case ($\eta = 0$) and then the shear wave velocity is (Deresiewicz 1960; Morency & Tromp 2008)

$$V_s = \sqrt{\frac{\mu}{\rho - \frac{\phi\rho_f}{T}}}. \tag{C5}$$